Plasmonic Silver Supercrystals with Ultrasmall Nanogaps for Ultrasensitive SERS-Based Molecule Detection

Cuifeng Tian, Yonghui Deng, Dongyuan Zhao, and Jixiang Fang**

Metallic periodic structures provide unique optical and photonic coupling effects. However, geometrically precise control of periodic structure is particularly challenging when studying scale at few nanometer. Here, a new class of highly ordered silver plasmonic supercrystals is successfully synthesized by means of a nanocasting process using ordered mesoporous silica as template. During the nanocasting via a chemical reduction, the diffusibility, viscosity, and strength of the reducing agents have an important influence on the formation of ordered superstructures. The silver superstructures demonstrate an excellent structural stability even after removing the silica template and a small nanogap of less than ≈2 nm between nanoparticles, which are very vital for light–matter coupling, giving rise to plasmonic hot spots. The silver plasmonic supercrystals exhibit an ultrahigh Raman enhancement with an average enhancement factor of ≈10^9 and an ultralow detection limit down to ≈0.1×10^{-15} M for diverse chemical and biological molecules. This novel template strategy to fabricate periodic plasmonic nanostructures can lead to a new class of plasmonic nanostructures and open extraordinary potentials for diverse applications.

1. Introduction

Geometrically precise control of metallic periodic structures provides unique optical and photonic coupling effects that promise applications in surface-enhanced Raman scattering (SERS), negative refraction, plasmonic waveguide, electromagnetic invisibility cloaks, and Fano resonance, etc.[1] SERS is a powerful molecular spectroscopy technique that exhibits great application potentials in analytical chemistry, environmental monitoring, medical diagnostics, and single molecule detection.[2] The SERS effect arises from light–matter interaction of metallic surfaces and incident light, which give rise to localized surface plasmon resonance. The plasmonic coupling effect at the nanometer gaps between metallic nanoparticles, i.e., the plasmonic hot spots, has also been utilized to further increase the SERS signals.[3] Extensive studies have been focused on creating hot spots spaced by small dielectric gaps of less than 10 nm. In addition to the original SERS platform made from electrochemically roughened surface,[4] a diverse novel SERS substrates have been developed, which include the well-ordered patterned arrays fabricated via lithographic techniques.[5] However, these techniques are limited by their low throughput, expensive operating cost, and small SERS active area. Importantly, it is still difficult to process small nanogaps down to sub-5 nm over large area. As such, size/shape controlled colloidal nanoparticles and their assemblies such as dimers, trimers, liner chains, core–satellite structures are attractive options due to the ability to synthesize through wet chemical approaches in bulk scale without the need of expensive instrumentation.[6] However, owing to the "coffee ring" effect, regulating the geometrical dimension, i.e., uniform nanoparticle gaps between colloidal nanoparticles via spontaneous aggregation or assembly are challenging.[7] With the assistance of surface ligands, nanoparticles can be assembled into superlattices,[8] but the introduction of polymer ligands unavoidably sacrifices the sensitivity of signals in a variety of applications, such as SERS, biosensors, plasmon-enhanced fluorescence. Therefore, the central problem is to homogeneously produce well-defined plasmonic structures that can reproducibly fabricate sub-5 nm nanogaps with controllable gap distance and enhanced hot spot density within the plasmonic structure.

In comparison with the nanoparticle superlattices obtained via self-assembly of metallic nanocrystals by means of the polymer ligands,[8] the ordered nanoparticle supercrystals may also be synthesized via replicating 3D colloidal (e.g., polymer or SiO_2 spheres) template[9] or ordered mesoporous silica (e.g., KIT-6, SBA-15, MCM-48) templates.[10] For example, 2D dimpled gold nanoplates were fabricated by vapor reduction using a 3D lattice of silica nanospheres (≈40 nm) as a template.[9] Unfortunately, the dimpled-type array is not suitable for the applications in SERS. Using ordered mesoporous silica (KIT-6 and SBA-15) template, Yamauchi's group has successfully fabricated polyhedral mesoporous Pt nanoparticles through a chemical reduction route.[10] However, the synthesis of highly

Dr. C. Tian, Prof. J. Fang
State Key Laboratory for Mechanical Behavior of Materials
School of Science
Xi'an Jiaotong University
Shann xi 710049, China
E-mail: jxfang@mail.xjtu.edu.cn
Prof. Y. Deng, Prof. D. Zhao
Department of Chemistry
Shanghai Key Laboratory of Molecular Catalysis and Innovative Materials Advanced Materials Lab
Fudan University
Shanghai 200433, China
E-mail: yhdeng@fudan.edu.cn

DOI: 10.1002/adom.201400576

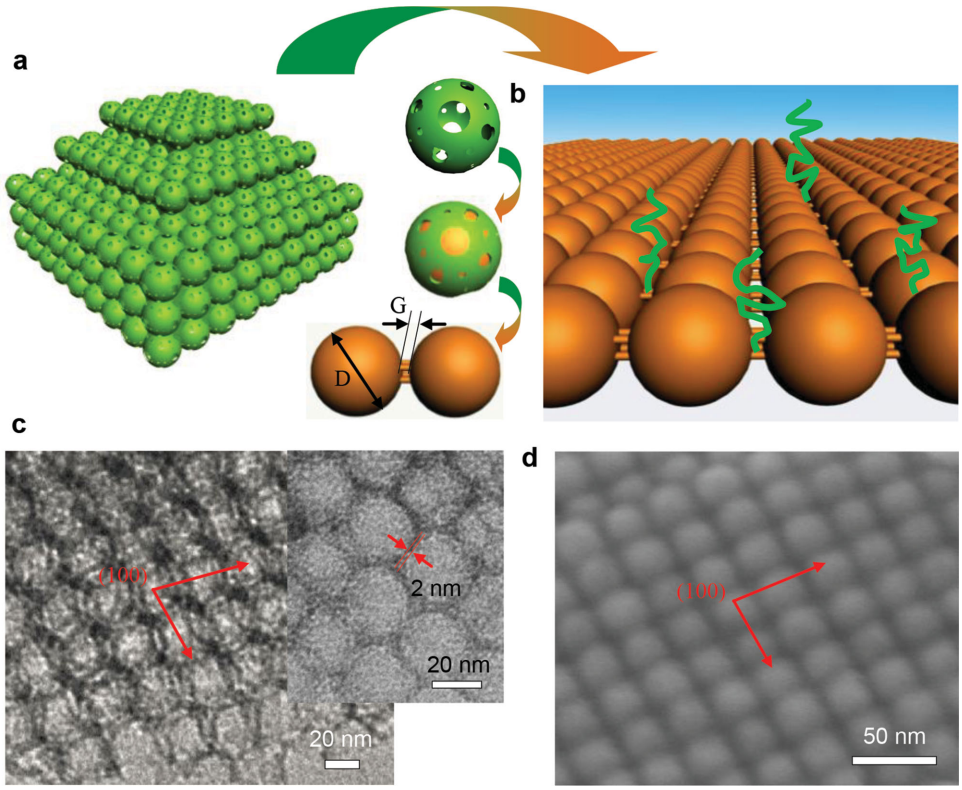

Figure 1. The ordered mesoporous template strategy to synthesize silver plasmonic supercrystals. a,b) Schematic diagram of the synthesis procedure for ordered silver supercrystals by means of a nanocasting process using different templates with a variety of pore size and wall thickness, c) TEM image of the template OMS-28, d) SEM image of OMASC-28.

ordered gold or silver supercrystals with well-controlled particle gaps via silica template protocol has not been reported. In particular, compared with the dimpled-type array reported in ref., [9] the current supercrystals with nanogap-type ordered structure would result in novel plasmonic coupling effects between nanoparticle building units.

Herein, for the first time, we report the fabrication of highly ordered Ag plasmonic supercrystals using ordered mesoporous silica with uniform spherical mesopores as a template through a chemical reduction approach. The template strategy (**Figure 1**a,b) briefly involves nanocasting of Ag nanostructures within the ordered mesopore nanoreactors and the removal of mesoporous silica. The current template protocol demonstrates several remarkable advantages for their applications in plasmonic nanooptics and nanophotonics. First, a highly stable structure with high density and uniform nanogaps can be reserved even after template removal owing to the unique mesopore structure of silica template. More importantly, a tunable nanogap size ("G") down to less than 2 nm can be created by means of thin wall thickness of silica template, which is vital for both SERS and tip-enhanced Raman spectroscopy (TERS) sensing, as well as other research related to plasmonic hot spots. Moreover, the replicating fabrication based on the nanocasting protocol using silica template is organic free, thus is a great benefit to the plasmonic enhancement. Our novel template strategy could lead to a new class of plasmonic nanostructures and open extraordinary potentials for diverse applications.

2. Results and Discussion

Ordered mesoporous materials are a kind of nanoporous molecular sieves with pores of 2.0–50 nm in diameter which are aligned in 2D or 3D arrays throughout the materials. This kind of materials possess high surface areas, large pore volume, and uniform mesopores, which endows them application potentials in catalysis, drug delivery, etc. On the other hand, the uniform mesopores are idea nanoreactors for templating synthesis of inverse nanomaterials with replicated structures.[11] In this work, we chose one class of ordered mesoporous silica as templates to prepare the ordered Ag supercrystals (denoted OMASC-28) with mesostructure features. The OMASC-28 silica template was synthesized through solvent evaporation-induced aggregating approach,[12] which displays tunable pore sizes from 10 to 50 nm and small wall thickness. Figure 1c shows the mesostructure of the ordered mesoporous silica templates (OMS-28) with a pore size of 28 nm. The transmission electron microscopy (TEM) image in Figure 1c indicates that the OMS-28 template has a highly ordered structure with preferable arrangement along the [100] direction. The wall thickness of OMS-28 is measured from TEM image (Figure 1c, inset) to be around ≈2 nm, consistent with the previous report.[12]

The OMASC-28 was synthesized by means of the nanocasting approach[13] through a chemical reduction process. Figure 1d shows the scanning electron microscopy (SEM) image of the OMASC-28 obtained via the OMS-28 template. From Figure S1 in the Supporting Information, it can be seen

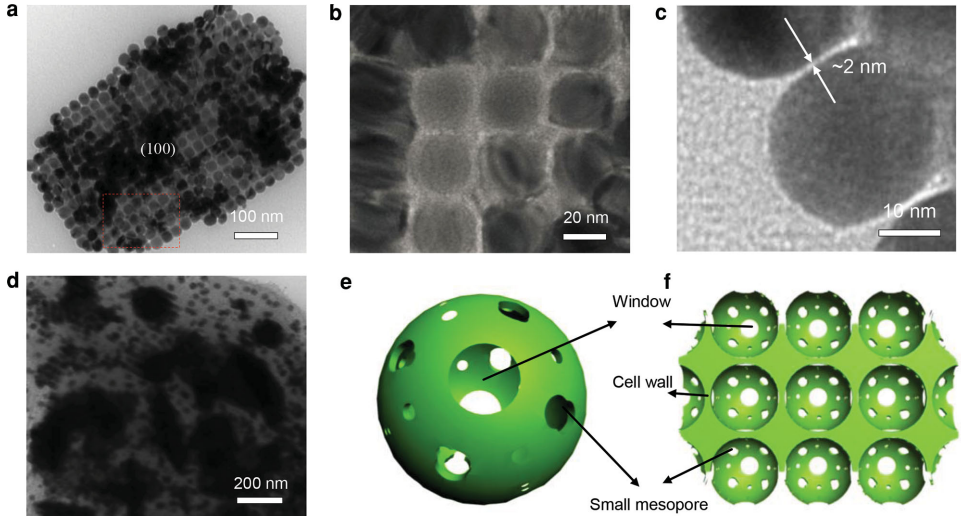

Figure 2. TEM images of the OMASC-28 and schematic plots of OMS-28. a–c) Low and high magnification TEM images of OMASC-28 after removal of template OMS-28. d) TEM image of OMASC-28 within OMS-28 template. e,f) Schematic plots of OMS-28 template, showing the unique dual-mesoporous structure consisting of large mesopores (window) and small wormlike mesopores and thin cell wall.

that the separated plate-like OMASC-28 shows the size around ≈1 μm. The Ag nanoparticles, as a replica, display a uniform size distribution of ≈28 nm, which is consistent with the pore size of the parent template. The OMASC-28 shows plate-like and tetragonal arrangement (Figure 1d and **Figure 2**a) of the Ag nanoparticle owing to the {100} preferred facet of the parent template (Figure S2, Supporting Information). One can note that some discrete nanoparticles land on the surface of Ag supercrystals (Figure 2a). It probably attributes to the overgrowth along nonpreferred {100} facet of template or the reabsorption of the discrete nanoparticles onto the surface of Ag supercrystals during removing template. The selected area electron diffraction (SAED) pattern (Figure S3, Supporting Information) taken from the boxed area of Figure 2a shows the polycrystalline feature of the plate-like Ag supercrystals, which is similar with previous explanation.[14] It is also worth noting that the plate-like OMASC-28 demonstrates a uniformly distributed nanogap (around 2 nm) between the nanoparticles (Figure 2b,c). The uniform nanogap sizes are consistent with the wall thickness of the parent template, OMS-28.[12] The template was removed thoroughly and confirmed by the energy dispersive X-ray spectrometry (EDS) line scan (Figure S4, Supporting Information), exhibiting no obvious localization of silicon or oxygen element within the nanogaps. In order to further analyze the silica residua after removing the template, X-ray photoelectron spectroscopy (XPS) of bulk sample has been performed. Figure S5, Supporting Information, reveals that the silica template may be removed completely after washing by NaOH solution three times.

To clarify the growth mechanism during the nanocasting process, diverse reducing agents have been investigated. When a relatively weak reduction agent was used, e.g., ethylene glycol (EG), some discrete OMASC-28 aggregates consisting of Ag nanoparticles with uniform size of ≈28 nm were observed within the pore channels of parent template (Figure 2d and Figure S6a,b, Supporting Information). However, in the case of the ascorbic acid (AA), a stronger reducing agent relative to EG, the deposited Ag nanoparticles exhibit only random distribution, and disordered structure can be found in the sample. Consequently, separated deposition within the pore channels and growth on the outer surface of the OMS-28 were observed (Figure S6c and S7a, Supporting Information). These results suggest that the use of EG is vital for the formation of OMASCs with well-ordered mesostructures. The reducing agent power-dependent filling capacity within the mesoporous silica is similar with the deposition of Pt polyhedral within KIT-6.[10] It is thus interesting to study whether the ordered mesostructural Ag supercrystals can also be obtained by using other weak reducing agents. To address this, a weak one relative to AA, but with high viscosity, the glucose was employed to synthesize the Ag supercrystals at relatively low temperature (353 K), which was supposed to offer a proper reducing power. In this situation, again, only Ag nanospheres with discrete distribution over the entire of the silica matrix were formed (Figures S6d and S7b, Supporting Information). Therefore, the ideal diffusivity, low viscosity, and appropriate reduction power are very important for the successful growth of highly ordered Ag supercrystals.

Based on these observations, we summarize the growth mechanism and structural feature of the OMASC-28 (Figure 2e,f, and Figure S8 and S9, Supporting Information). Briefly, the layer-by-layer assembled structure of OMS-28 probably with {100} preferred planes (Figure 1c and Figure S2, Supporting Information) would be preferable to form the 2D plate-like ordered mesostructural Ag supercrystals (Figure 2a and Figure S1, Supporting Information).[12] The nanoparticle building units in OMASC-28 were found to have hollow-shell or multigrained structures like previous reports,[15] but the solid nanospheres and single crystalline structure. This could be attributed to several factors including extremely high Ag precursor concentration (i.e., 3 M), different kinds of reduction agent species and the high mobility of reduction agents within the parent template driven by heating. In fact, previous studies have also suggested that the interior surface feature and

mesochannel structure of silica template, reaction conditions as well as reduction agent species all highly influence the growth speed and mobility of precursors within the silica mesoporous matrix, thus the structure of product.[16] In this study, the OMS-28 template shows a unique hierarchical mesostructure in the wall of the silica cells, consisting of large mesopores (window) and small wormlike mesopores (Figure 1c,e,f). This unique dual-mesoporous structure provides a plenty of highly interconnected pore channels, hence enhance the mobility of precursors. Moreover, by means of the nanocasting process, these interconnected pore channels may create nanobridges between particles (Figure 2f and Figure S9, Supporting Information), which ensure the structural stability of Ag supercrystals even after removal of the silica template.[12] Importantly, the ultrathin wall (≈2 nm) of the OMS-28 template combining with the dual-mesoporous structure make the OMASC-28 Ag supercrystals a novel nanogap mode, where the nanoparticle building units are separated by gaps of only ≈2 nm and connected by small fine nanoparticles (nanobridges) with less than 2 nm in size (Figure S9, Supporting Information).

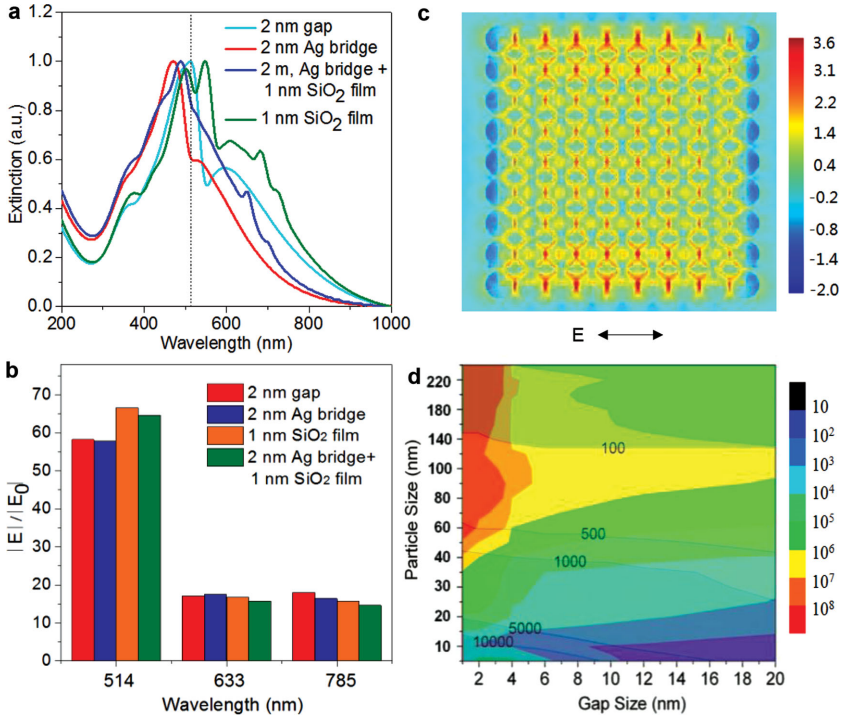

Figure 3. The FDTD calculation of OMASC-28. a) Calculated UV–vis–NIR spectra of OMASC-28 with various gap modes. b) Histograms of field enhancements of OMASC-28 for various gap modes calculated at excitation wavelengths of 514, 633, and 785 nm, respectively. c) Calculated *E*-field distributions for OMASC-28 and their *E*-field intensity. d) The *E*-field enhancement and hot spot density with an excitation wavelength of 514 nm, as a function of nanoparticle sizes and gap sizes. The right scale bar in d) represents the values of *E*-field enhancement, and the number marked on the contour map is the hot spot density.

To understand the interactions of an electromagnetic wave with the OMASC-28, a finite difference time-domain (FDTD) calculation was applied, and the results were compared with those for diverse particle sizes ("D") and gap modes including insulated gap, bridge mode as well as a thin SiO_2 film-coated gap mode (Figure S10, Supporting Information). The results show that the plasmon resonance highly depends on the "D" and the gap modes. Under a constant "G" of 2 nm, the calculated UV spectra of OMASCs with various "D" (i.e., 10, 20, 28, and 38 nm) exhibit relatively wide plasmon bands from 400 to 530 nm (Figure S11, Supporting Information), respectively. However, under a constant "G" of 2 nm and constant "D" of 28 nm, diverse gap modes result in a slight changes of plasmon bands from 470 to 550 nm (**Figure 3**a). For example, compared with the insulated gap, the bridged mode demonstrates a slightly blue-shifted resonant peak, and the coating of SiO_2 film leads to a red-shift. Thus, in the practical application, we may adjust the geometrical dimensions of OMSs to synthesize OMASCs and meet the requirement of laser wavelengths. Furthermore, the incident wavelength dependence of the field enhancements for diverse gap modes at 514, 633, and 785 nm, were calculated, respectively. One can see that, the bridged mode coated by SiO_2 film demonstrates the highest field enhancement with $|E|/|E_0|\approx 66.6$ at excitation wavelength of 514 nm, which corresponds to a SERS enhancement (proportional to $\approx |E|^4$) of $\approx 10^7$ (Figure 3b). Figure 3c shows the calculated electromagnetic field distribution of OMASC-28 with diverse gap modes at the 514 nm incident laser wavelengths. Clearly, the electromagnetic enhancement is highly localized in the gap region between nanoparticles around the entire Ag arrays.

The OMASCs is an ideal model system to investigate the influence of "D," "G" and gap modes on the electromagnetic field enhancement, and to examine how to select an optimized "D" to maximize the hotspot density and signal enhancement, simultaneously. To shed light on the interaction among these factors, the field enhancement (Figure S12a, Supporting Information) and the hot spot density (Figure S12b, Supporting Information) depending on "D" and "G" were investigated. Figure 3d shows the overlapping contours of the *E*-field enhancement and hot spot density depending on "D" and "G." It is found that the smaller particle and gap size, the higher hot spot density may be obtained (Figure S12c, Supporting Information). However, for the *E*-field enhancement, a small gap size is favorable. Meanwhile, the highest *E*-field enhancement locates in a range of "D" above 60 nm (Figure S12d, Supporting Information). In this regard, the ordered porous silica template protocol (by designing diverse pore structure and size) will open tremendous potential to fabricate Ag nanoparticle supercrystals with tailored "D" and "G," and hence meet various applications using the SERS technique.

In order to evaluate the SERS sensitivity of the OMASC-28, the SERS response was examined by using crystal violet (CV) dye as the probe molecule, which has also been widely used in previous experiments[17] and our recent studies.[18] To precisely

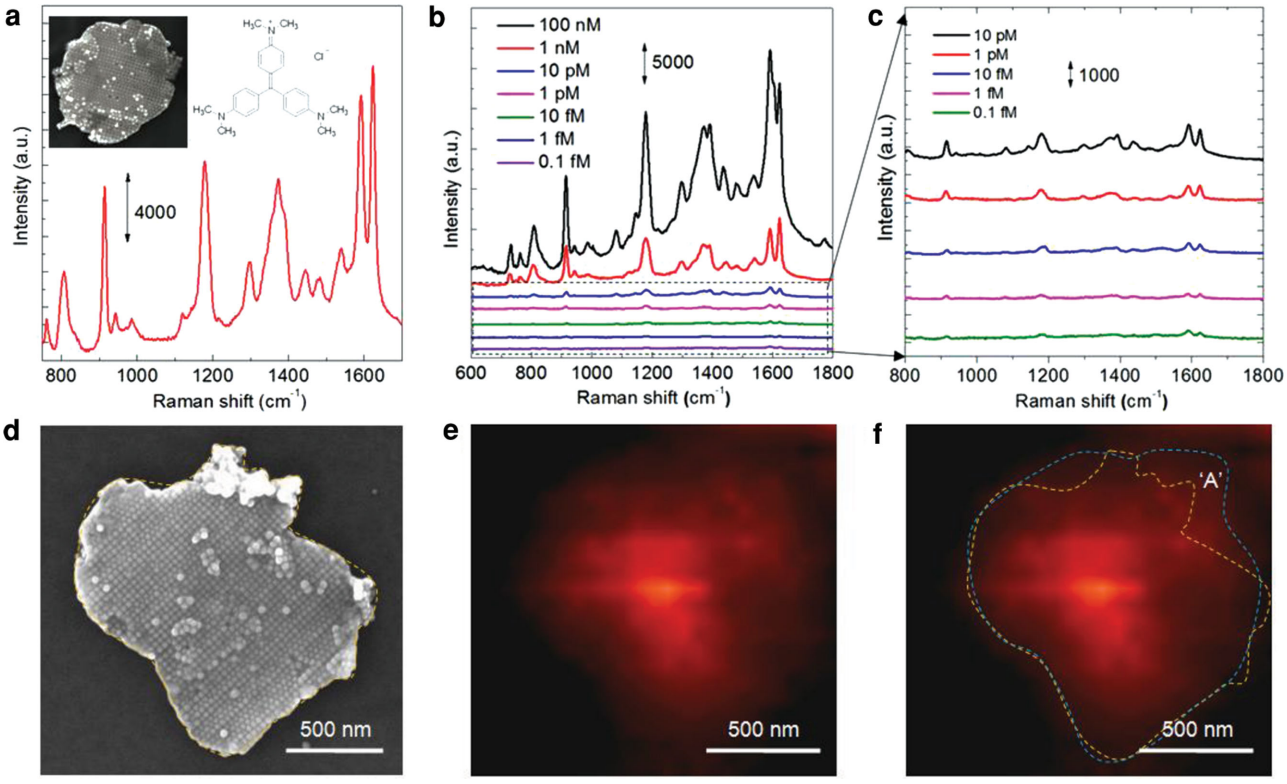

Figure 4. SERS performance of OMASC-28 with CV dye as probe molecules. a) SERS spectra measured at the CV concentration of 10^{-7} M and excitation wavelength of 514 nm with 2 s acquisition time. The inset SEM image is the measured OMASC-28 sample. b,c) SERS spectra measured at CV concentrations ranging from 0.1×10^{-15} M to 100×10^{-9} M. d–f) A SEM image of plate-like OMASC-28 and the corresponding Raman image recorded by mapping the CV Raman peak at ≈1172 cm^{-1}.

determine the structural dependence on SERS activity, a silicon wafer patterned by electron beam lithography was employed as a substrate to support OMASC-28 so as to ensure that the exact same particle is characterized (Figure S13, Supporting Information). **Figure 4**a demonstrates the Raman spectrum measured by using a 514 nm incident laser with a 10^{-7} M CV aqueous (20 μL) dropping on the marked silicon substrates with OMASC-28 predeposited. According to the procedure and assumptions described previously[19] and also used in our previous experiments[18] for the CV molecules, the average enhancement factor (EF) of the OMASC-28 was estimated about ≈1.22×10^9 under the 514 nm excitation wavelength (see details in the Supporting Information). The EF value for OMASC-28 is highly remarkable among the reported SERS substrates.[20] Meanwhile, the Raman signals demonstrate a relatively small dispersion with a standard deviation of ≈17.1% if considering the ratio between the signal intensity and the actual area of OMASC-28 specimens. In addition, the measured EF value is two orders of magnitude higher than the calculated one. This is acceptable, because chemical enhancement and surface roughness factors can be involved in actual experiments.[21] Similarly, the discrepancy between experimentally measured and calculated EF value has also been observed in many previous literatures.[18a,20] To explore the limit of detection (LOD) for the OMASC-28, a series of low concentrations of CV aqueous solution ranging from 100×10^{-9} M to 0.1×10^{-15} M were measured. From Figure 4b,c, we observe that the LOD of OMASC-28 for CV molecule can reach ≈0.1×10^{-15} M. Figure 4d–f shows the SEM-correlated nano-Raman images by mapping the characteristic Raman peak of CV at 1172 cm^{-1}. Although the Raman image may not provide precise information of hot spots due to the limited resolution, it still suggests that the Raman dye may present in the mapping area. If compare Raman image in Figure 4f with the corresponding SEM image (Figure 4d), one can find that these images show the similar profile (dashed–dotted circle), revealing the CV molecules may uniformly distribute over the entire surface of OMASC-28. Note that the up-right region "A" of the Raman image displays a large difference as that in SEM, which could be attributed to the interaction between the detected OMASC-28 and the aggregate shown in Figure S14 in the Supporting Information.

To further demonstrate the current protocol toward a universal SERS platform, we also examined diverse molecules under similar conditions. First, an anionic dye Congo red (CR) was tested. The Raman fingerprint peaks of phenyl–*N*= stretching at 1158 cm^{-1}, naphthyl aromatic ring at 1376 cm^{-1}, phenyl ring at 1598 cm^{-1}, respectively, can be identifiable at the CR concentration of 1×10^{-12} M. However, these peaks cannot be distinguished when the concentration down to 10×10^{-15} M (**Figure 5**a). The second molecule was *p*-mercaptoaniline (pMA), which has a thiol group substituted at the para position of aniline not only forms a self-assembled monolayer (SAM) on metal surfaces but also is an important surface probe

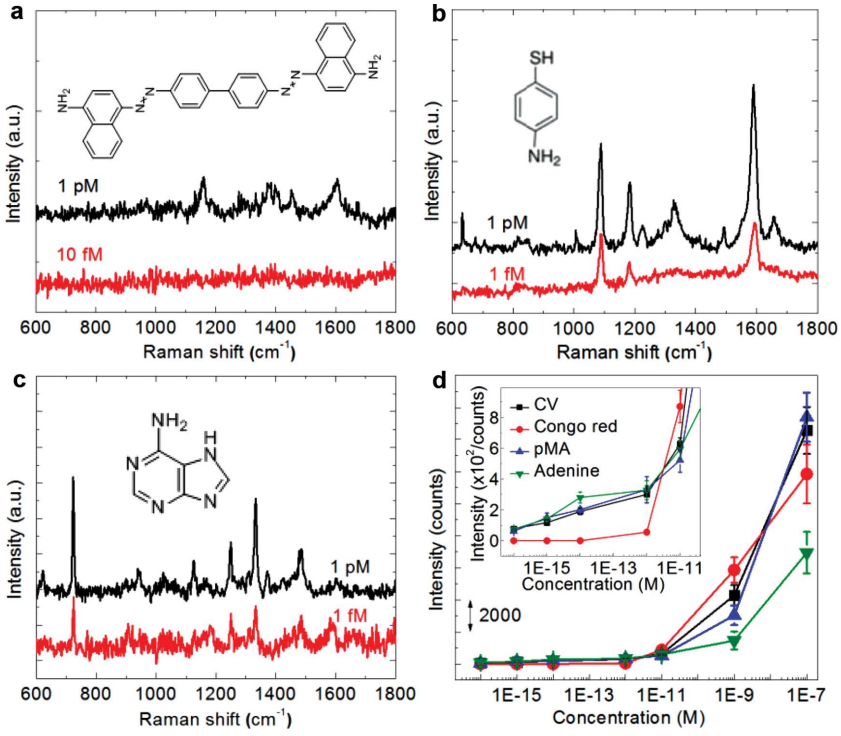

Figure 5. SERS performance of OMASC-28 with different probe molecules. a–c) SERS spectra for different molecules, a) Congo red, b) p-MA, c) adenine. d) SERS intensity at concentrations ranging from 0.1×10^{-15} M to 100×10^{-9} M for various dye molecules. The curves below 10×10^{-12} M are magnified for clarity.

molecule in SERS. From Figure 5b, the characteristic bands of pMA are clearly visible even at low concentrations from 1×10^{-12} M to 0.1×10^{-15} M. Third, the application of OMASC-28 is then extended to detect the biological analyte, e.g., adenine, a DNA base molecule. Adenine is one of the two purine nucleobases, which is an ideal molecule to test the biosensing capability of OMASC-28 due to the number of biomolecules that contain adenine. The investigation of adenine is extremely important due to its high level of nonspecific binding to metal surfaces and the label-free detection of DNA hybridization.[22] Figure 5c shows many of the spectral features of adenine along with the characteristic purine-ring breathing mode at 736 cm^{-1} and stretching modes of various CN bonds at around 1333 cm^{-1} at the concentrations even down to 0.1×10^{-15} M. This LOD value is 3–4 orders of magnitude higher than that in recent reports on ultralow concentration detection of adenine molecules.[23]

The correlation of SERS intensities with analyte concentrations for diverse dye molecules (Figure 5d, Figure S15, Supporting Information, and Figure 16) displays Langmuir isotherm curves with nonlinear least-squares regression.[24] The experimental data were obtained using at least three independent specimens for each concentration, achieving reliable measurements with less than 30% SERS intensity variation. When many more molecules are present in detected solution, a linear relation between SERS intensity and the concentration can be observed in the range of 100×10^{-9} M to 10×10^{-12} M (Figure 5d). However, the Langmuir isotherm behavior (Figure S16, Supporting Information) might indicate sub-monolayer or monolayer adsorption of dye molecules on the surface of OMASC-28 particularly at an ultralow concentration, e.g., from 10×10^{-12} M to 0.1×10^{-15} M. Thus, the SERS signal intensities change a little at a concentration below 10×10^{-12} M, implying that only a few dye molecules residing in the nanogaps can exhibit efficient Raman enhancement. This nonlinear behavior is also consistent with previous reports.[24b,25] According to above results, the superior sensitivity and LOD we obtained could be attributed to various factors since SERS technique is complex system involving the interactions between light-molecule, light-surface as well as surface-molecule. However, beside of the well-defined nanogaps (≈2 nm) and the intrinsic character of detected molecules, the adsorption capability of the detected molecule onto the metal surface might be also important.[26] The measurement of zeta potential (ζ) shows that the surface of OMASC-28 is negatively charged with a value of ζ at around −24 mV (Figure S17, Supporting Information). Thus, electrostatic interactions might assist in increasing the affinity of probe molecules with our SERS substrate, therefore improving the SERS sensing detection and result in the different LOD for diverse analytes.[26]

3. Conclusions

In summary, for the first time, we have successfully employed the ordered porous silica as templates to synthesize a new class of optically tunable plasmonic supercrystals through a chemical reduction approach. A highly stable mesostructure, i.e., high density and uniform nanogaps, can be reserved even after removing the template. More importantly, a tunable nanogap size down to 2 nm even less can be achieved, which is very vital for the communities of both SERS and TERS as well as other researches related to plasmonic hot spots. The formation mechanism of ordered silver nanoparticle supercrystals was investigated, using diverse reducing agents. It is found that, the diffusivity and reduction speed with various reducing agents play a crucial role in the successful growth of long-range ordered silver supercrystals within the parent template. The Raman spectroscopy measurements indicate that silver supercrystals of OMASC-28 as SERS substrate have an ultrahigh sensitivity on the magnitude of $\approx 10^9$. Meanwhile, a lowest detection limit down to $\approx 0.1 \times 10^{-15}$ M for CV, pMA and adenine molecules reported to date, has been achieved, which enables the detection of a single or a few molecules. Therefore, the current template strategy, as a seminal piece of work, could lead to a new class of plasmonic nanostructures and open extraordinary potentials for diverse applications, such as biosensing, catalyst, and SERS-based detection.

4. Experimental Section

Materials: Silver nitrate ($AgNO_3$), crystal violet ($C_{25}H_{30}ClN_3$), and adenine ($C_5H_5N_5$) was purchased from Sigma. Ethylene glycol (EG) ($HOCH_2$–CH_2OH), ascorbic acid ($C_6H_8O_6$), glucose ($C_6H_{12}O_6$), ethanol (C_2H_5OH), and sodium hydroxide (NaOH) were purchased from Tianjin Chemical Corp. Congo red ($C_{32}H_{22}N_6Na_2O_6S_2$) was purchased from Tianjin Kermel Chemical Reagent Co., Ltd. p-mercaptoaniline (C_6H_7NS) was purchased from Alfa Aesar.

Synthesis of Ordered Mesoporous Silica (OMS-28): The ordered mesoporous silica was synthesized via the solvent evaporation-induced aggregating assembly (EIAA) method reported previously.[1] For a typical preparation, 7.0 g of EO_{125}-*b*-MMA_{174} dissolved in THF solution (0.57 wt%) was mixed with 2.0 g of 2 M HCl solution with stirring. Then, 0.30 g of TEOS was added into the above transparent solution, the composition of EO_{125}-*b*-MMA_{174}/ THF/2M HCl/TEOS mass ratio was 1:175:50:7.5. After that, the solution was left to stand for evaporation of THF at 25 °C in air in a hood. After 48 h, white silica/PEO-*b*-PMMA composites were precipitated from the solution and collected by centrifugation, washed with water for three times, and dried at 25 °C. The as-made sample was hydrothermally treated at 100 °C for 24 h, and then calcined at 550 °C in air for 5 h to remove the template.

Synthesis of Ordered Mesostructural Silver Supercrystals (OMASC-28) by the Chemical Reduction Method: In order to obtain ordered silver supercrystals, the OMS-28 was used as template. In the dipping process, 0.0035 g of OMS-28 powder was immersed into $AgNO_3$ aqueous solution (3 M, 21 μL) using an incipient wetness method. After the sample drying at 313 K for 2 d in the vacuum oven, 45 μL of EG was dropped on the sample. The sample was then placed in another flat vessel for heating at 393 K in oil bath for 3 min. The color of the sample was gradually changed to white gray. After the reduction process, the composite material was stay in the vessel for ≈12 h. Then the template was completely removed by treating the composite material with 3 M NaOH solution three times at 273 K. Finally, the ordered silver material thus obtained was washed with distilled water and ethanol several times and dried at room temperature.

As for the other reduction agents, such as ascorbic acid (AA, 3 M) and glucose, the only difference is the reduction process. The volume ratio of $AgNO_3$ and AA was 1:1 and the reduction process performed at room temperature. The volume ratio of $AgNO_3$ and glucose was 3:5 and the reduction process carried out at the temperature 353 K for 30 min.

Preparation of the SERS Samples: To prepare the SERS substrate, three steps were used. i) dropping one layer of OMASC-28 onto the silicon wafer (6 mm × 6 mm), ii) preparing different solution of dyes, the aqueous solutions of CV and Congo red with different concentrations were prepared, respectively. The ethanol solutions of PMA and Adenine were prepared at different concentrations of 10^{-16}, 10^{-15}, 10^{-14}, 10^{-12}, 10^{-11}, 10^{-9}, and 10^{-7} M. Then, iii) 20 μL of dye solution were added onto the substrate of OMASC-28, and dried with nitrogen gas. For the detection limit measurements, the SERS substrates were immersed into different dye molecules with various concentrations for 2 h, then washed in ethanol to remove excess molecules, and finally dried with nitrogen gas.

Characterization: The morphology and structure of OMS-28 and OMASC-28 was observed by scanning electron microscopy (SEM) (JSM-7000F) and a transmission electron microscopy (TEM) (JEM 2100). X-ray photoelectron spectroscopy (XPS) (Thermo VG K-alpha, UK) was used to investigate the surface elemental composition of OMASC-28 and the photoelectrons generated by Al Kα source (1486.6 eV). Raman spectra measurements were performed with a confocal Raman spectroscopy (LabRAM HR800) at the excitation wavelength of 514 nm from an argon ion laser, the grating was 600 g mm^{-1}. The laser spot on a sample was ≈0.8 μm in diameter under confocal mode. Raman signals were collected through the same objective (100×) in the back-scattering geometry. For measuring CV dye of 10^{-7} M, the laser power was ≈0.022 mW and the acquisition time was 2 s. For measuring other concentrations of CV and other dyes, the laser power was ≈0.032 mW and the acquisition time was 10 s. The AFM image was made in the tapping mode with a Vit-p tip using a NT-MDT AFM controller. AFM-correlated nano-Raman images were recorded by mapping the characteristic Raman peak of CV at 1172 cm^{-1} via the AFM (NT-MDT) connected with a Raman spectrometer (NT-MDT) equipped with a 532 nm solid state laser, using a laser power of 0.12 mW, step size of 30 nm, scan area of 1.9 μm × 1.9 μm, acquisition time of 0.5 s/points. The zeta potential was measured using a Zeta Sizer Nano ZS (ZEN 3690, Malvern, UK).

Supporting Information

Supporting Information is available from the Wiley Online Library or from the author.

Acknowledgements

This work was supported by National Natural Science Foundation of China (Nos. 51171139 and 51372041), the New Century Excellent Talents in University (NCET-10–11 and NCET-12–0123), the Scientific New Star Program in Shann Xi Province (No. 2012KJXX-03), the Fundamental Research Funds for the Central Universities (Nos. xkjc2014004 and 08142008), the specialized research fund for the doctoral program of higher education of China (20130201110032 and 20120071110007), the innovation program of Shanghai Municipal Education Commission (13ZZ004), and the Shanghai Rising Star Project of STCSM (12QH1400300). The authors would like to thank Professor Xinyi Lin for helpful discussion.

Received: December 3, 2014
Revised: December 4, 2014
Published online: January 2, 2015

[1] a) S. F. Tan, J. K. W. Yang, P. Bai, M. Bosman, C. A. Nijhuis, *Science* **2014**, *343*, 1496; b) C. Ciraci, R. T. Hill, J. J. Mock, Y. Urzhumov, A. I. Fernandez-Dominguez, S. A. Maier, J. B. Pendry, A. Chilkoti, D. R. Smith, *Science* **2012**, *337*, 1072; c) Z. Y. Li, Y. N. Xia, *Nano Lett.* **2010**, *10*, 243.

[2] a) J. F. Li, Y. F. Huang, Y. Ding, Z. L. Yang, S. B. Li, X. S. Zhou, F. R. Fan, W. Zhang, Z. Y. Zhou, D. Y. Wu, B. Ren, Z. L. Wang, Z. Q. Tian, *Nature* **2010**, *464*, 392; b) R. Zhang, Y. Zhang, Z. C. Dong, S. Jiang, C. Zhang, L. G. Chen, L. Zhang, Y. Liao, J. Aizpurua, Y. Luo, J. L. Yang, J. G. Hou, *Nature* **2013**, *498*, 82; c) D. K. Lim, K. S. Jeon, H. M. Kim, J. M. Nam, Y. D. Suh, *Nat. Mater.* **2010**, *9*, 60; d) M. P. Cecchini, V. A. Turek, J. Paget, A. A. Kornyshev, B. Joshua, *Nat. Mater.* **2013**, *12*,165; e) P. H. C. Camargo, M. Rycenga, L. Au, Y. N. Xia, *Angew. Chem. Int. Ed.* **2009**, *48*, 2180; f)W. Y. Li, P. H. C. Camargo, X. M. Lu, Y. N. Xia, *Nano Lett.* **2009**, *9*, 485.

[3] a) H. X. Xu, E. J. Bjerneld, M. Kall, L. Borjesson, *Phys. Rev. Lett.* **1999**, *83*, 4357; b)H. X. Xu, J. Aizpurua, M. Kall, P. Apell, *Phys. Rev. E* **2000**, *62*, 4318.

[4] a) M. Fleischmann, P. J. Hendra, A. J. McQuillan, *Chem. Phys. Lett.* **1974**, *26*, 163; b) D. L. Jeanmaire, R. P. Van Duyne, *J. Electroanal. Chem. Interfacial Electrochem.* **1977**, *84*, 1.

[5] a) E. J. Smythe, M. D. Dickey, J. Bao, G. M. Whitesides, F. Capasso, *Nano Lett.* **2009**, *9*, 1132; b) F. S. Ou, M. Hu, I. Naumov, A. Kim, W. Wu, A. M. Bratkovsky, X. Li, R. S. Williams, Z. Li, *Nano Lett.* **2011**, *11*, 2538; c) H. C. Jeon, C. J. Heo, S. Y. Lee, S. M. Yang, *Adv. Funct. Mater.* **2012**, *22*, 4268.

[6] a) H. Wang, L. Chen, Y. Feng, H. Chen, *Acc. Chem. Res.* **2013**, *46*, 1636; b) N. Gandra, A. Abbas, L. Tian, S. Singamaneni, *Nano Lett.* **2012**, *12*, 2645.

[7] A. Q. Chen, A. E. Deprince III, A. Demortiere, A. Joshi-Imre, E. V. Shevchenko, S. K. Gray, U. Welp, V. K. Vlasko-Vlasov, *Small* **2011**, *7*, 2365.

[8] a) N. Nishida, E. S. Shibu, H. Yao, T. Oonish, K. Kimura, T. Pradeep, *Adv. Mater.* **2008**, *20*, 4719; b) T. Thai, Y. Zheng, S. H. Ng, S. Mudie, *Angew. Chem. Int. Ed.* **2012**, *51*, 8732; c) R. A. Alvarez-Pueblaa, A. Agarwal, P. Manna, B. P. Khanal, P. Aldeanueva-Potel, E. Carbó-Argibay, N. Pazos-Pérez, L. Vigderman, E. R. Zubarev, N. A. Kotova, L. M. Liz-Marzán, *Proc. Natl. Acad. Sci. USA* **2011**, *108*, 8157; d) J. Henzie, M. Grunwald, A. Widmer-Cooper, P. L. Geissler, P. D. Yang, *Nat. Mater.* **2011**, *11*, 131.

[9] a) Y. Kuroda, K. Kuroda, *Angew. Chem. Int. Ed.* **2010**, *49*, 6993; b) Y. Kuroda, Y. Sakamoto, K. Kuroda, *J. Am. Chem. Soc.* **2012**, *134*, 8684.

[10] a) H. J. Wang, H. Y. Jeong, M. Imura, L. Wang, L. Radhakrishnan, N. Fujita, T. Castle, O. Terasaki, Y. Yamauchi, *J. Am. Chem. Soc.* **2011**, *133*, 14526; b) M. H. Huang, A. Choudrey, P. Yang, *Chem. Commun.* **2000**, *36,* 1063; c) J. K. Shon, S. S. Kong, J. M. Kim, C. H. Ko, M. Jin, Y. Y. Lee, S. H. Hwang, J. A. Yoon, J. N. Kim, *Chem. Commun.* **2009**, *45,*650; d) L. Z. Wang, J. L. Shi, W. H. Zhang, M. L. Ruan, J. Yu, D. S. Yan, *Chem. Mater.* **1999**, *11*, 3015.

[11] a) D. Y. Zhao, J. L. Feng, Q. Huo, N. Melosh, G. H. Fredrickson, B. F. Chmelka, G. D. Stucky, *Science* **1998**, *279*, 548; b) Y. H. Deng, J. Wei, Z. K. Sun, D. Y. Zhao, *Chem. Soc. Rev.* **2013**, *42*, 4054; c) M. Kruk, *Acc. Chem. Res.* **2012**, *45*, 1678.

[12] a) J. Wei, H. Wang, Y. H. Deng, Z. K. Sun, L. Shi, B. Tu, M. Luqman, D. Y. Zhao, *J. Am. Chem. Soc.* **2011**, *133*, 20369; b) J. Wei, Q. Yue, Z. K. Sun, Y. H. Deng, D. Y. Zhao, *Angew. Chem. Int. Ed.* **2012**, *51*, 6149.

[13] a) H. Yang, D. Zhao, *J. Mater. Chem.* **2005**, *15*, 1217; b) R. Ryoo, S. H. Joo, S. Jun, *J. Phys. Chem. B* **1999**, *103*, 7743; c) A.-H. Lu, F. Schüth, *Adv. Mater.* **2006**, *18*, 1793.

[14] J. X. Fang, P. Kong, B. J. Ding, X. P. Song, Y. Han, H. Hahn, H. Gleiter, *Appl. Phys. Lett.* **2008**, *93*, 53115.

[15] a) B. Mandlmeier, J. M. Szeifert, D. Fattakhova-Rohlfing, H. Amenitsch, T. Bein, *J. Am. Chem. Soc.* **2011**, *133*, 17274; b) A. Takai, Y. Doi, Y. Yamauchi, K. Kuroda, *J. Phys. Chem. C* **2010**, *114*, 7586.

[16] M. H. Huang, A. Choudrey, P. D. Yang, *Chem. Commun.* **2000**, *36,* 1063.

[17] L. F. Zhang, S. L. Zhong, A. W. Xu, *Angew. Chem. Int. Ed.* **2013**, *52*, 645.

[18] a) J. X. Fang, S. Y. Du, S. Lebedkin, Z. Y. Li, R. Kruk, M. Kappes, H. Hahn, *Nano Lett.* **2010**, *10*, 5006; b) J. X. Fang, S. Y. Liu, Z. Y. Li, *Biomaterials* **2011**, *32*, 4877; c) C. F. Tian, C. H. Ding, S. Y. Liu, S. C. Yang, X. P. Song, B. J. Ding, Z. Y. Li, J. X. Fang, *ACS Nano* **2011**, *5*, 9442.

[19] a) Y. Wang, M. Becker, L. Wang, J. Q. Liu, R. Scholz, J. Peng, U. Gösele, S. H. Christainsen, D. H. Kim, M. Steinhart, *Nano Lett.* **2009**, *9*, 2384; b) W. B. Cai, B. Ren, X. Q. Li, C. X. She, F. M. Liu, X. W. Cai, Z. Q. Tian, *Surf. Sci.* **1998**, *406*, 9.

[20] D. K. Lim, K. S. Jeon, J. H. Hwang, H. Kim, S. Kwon, Y. D. Suh, J. M. Nam, *Nat. Nanotechnol.* **2011**, *6*, 452.

[21] a) P. Hildebrandt, M. Stockburger, *J. Phys. Chem.* **1984**, *88*, 5935; b) K. L. Wustholz, A. I. Henry, R. G. F. Mcmahon, N. Valley, M. E. Piotti, M. J. Natan, G. C. Schatz, R. P. Van Duyne, *J. Am. Chem. Soc.* **2010**, *132*, 10903.

[22] a) A. Barhoumi, N. J. Halas, *J. Am. Chem. Soc.* **2010**, *132*, 12792; b) R. Huang, H. T. Yang, L. Cui, D. Y. Wu, B. Ren, Z. Q. Tian, *J. Phys. Chem. C* **2013**, *117*, 23730; c) M. Chirumamilla, A. Toma, A. Gopalakrishnan, G. Das, R. P. Zaccaria, R. Karhne, E. Rondanina, M. Leoncini, C. Liberale, F. D. Angelis, E. D. Fabrizio, *Adv. Mater.* **2014**, *26*, 2353.

[23] a) H. Im, K. C. Bantz, S. H. Lee, T. W. Johnson, C. L. Haynes, S. H. Oh, *Adv. Mater.* **2013**, *25*, 2678; b) S. Cherukulappurath, S. H. Lee, A. Campos, C. L. Haynes, S. H. Oh, *Chem. Mater.* **2014**, *26*, 2445.

[24] a) H. L. Liu, Z. L. Yang, L. Y. Meng, Y. D. Sun, J. Wang, L. B. Yang, J. H. Liu, Z. Q. Tian, *J. Am. Chem. Soc.* **2014**, *136*, 5332; b) H. K. Lee, Y. H. Lee, I. Y. Phang, J. Q. Wei, T. X. Liu, X. Y. Ling, *Angew. Chem. Int. Ed.* **2014**, *53*, 5054.

[25] Y. B. Guo, M. K. K. Oo, K. Reddy, X. D. Fan, *ACS Nano* **2012**, *6*, 381.

[26] a) X. L. Wang, R. L. Zong, S. K. Shi, Y. F. Zhu, *Anal. Meth.* **2014**, *6*, 4130; b) R. A. Alvarez-Puebla, R. F. Aroca, *Anal. Chem.* **2009**, *81*, 2280; c) S. L. Tan, M. Erol, S. Sukhishvili, D. Du, *Langmuir* **2008**, *24*, 4765.